

Tectonic–astronomical interactions in shaping late Paleozoic climate and organic carbon burial

Received: 26 March 2025

Accepted: 27 August 2025

Published online: 02 October 2025

 Check for updatesRen Wei^{1,2}, Zhijun Jin^{1,2}✉, Mingsong Li², Shuai Yuan³, Yongyun Hu³, Lin Dong², Rui Zhang⁴ & Juye Shi⁵

Tectonic processes and astronomical cycles are key drivers of Earth's climate and carbon systems. However, their interplay in shaping late Paleozoic climate variability remains poorly constrained. Here, we divide the late Paleozoic (~360–250 Ma) into three distinct tectonic phases based on full-plate tectonic reconstructions, geochemical datasets, and carbon cycle modeling, thereby elucidating how global sea levels and organic carbon burial responded to astronomically forced climate fluctuations under different tectonic phases. Our results show that intervals spanning ~360–330 Ma and ~280–250 Ma were characterized by elevated atmospheric CO₂ levels and intensified tectonic activity, which coincided with heightened climate variability and reduced regularity in orbitally paced sea-level changes. In contrast, during ~330–280 Ma, multiple proxies indicate reduced tectonic forcing and lower CO₂ concentrations, which were accompanied by more stable climate conditions and clearer expression of astronomical cycles. These conditions facilitated rhythmic deposition and widespread organic carbon burial.

The late Paleozoic (~360 to 250 Ma) was a transformative period in Earth's history, marked by extensive tectonic reorganization, the formation of the supercontinent Pangaea, widespread glaciation, and significant shifts in global climate and sea levels^{1,2}. These processes not only reshaped Earth's surface but also played pivotal roles in driving carbon cycling and altering biological productivity^{3–6}. Notably, this era witnessed the formation of extensive organic-rich shales and coal deposits^{7,8}, which served as a major mechanism for carbon sequestration, contributing to long-term reductions in atmospheric CO₂ and potentially driving global cooling^{9–11}. These deposits today represent a substantial portion of Earth's fossil fuel reserves, underpinning significant global energy resources. Understanding the driving forces behind climate and carbon cycle dynamics during this period is therefore essential for reconstructing how the Earth system responded and for appreciating the origins and distribution of key fossil resources.

Over the past few decades, substantial progress has been made in elucidating the impact of tectonic processes on global climate, including subduction zone activity, mid-ocean ridge expansion, and large igneous province eruptions^{12,13}. These tectonic drivers influenced atmospheric CO₂ levels through processes such as volcanic outgassing, silicate weathering, and the reorganization of oceanic circulation^{14,15}. By altering the distribution of continents and ocean basins, tectonics further modulated coupled ocean–atmosphere dynamics, thereby affecting regional and global climate systems¹⁶. Simultaneously, the relatively stable components of Earth's astronomical forcing, particularly eccentricity, have long been fundamental to understanding past climate variations¹⁷, as they modulate solar radiation received at Earth's surface and profoundly influence global climate states^{18,19}. Under relatively stable conditions, these orbital cycles are expected to produce distinct and continuous sedimentary

¹Institute of Energy, Peking University, Beijing, China. ²School of Earth and Space Sciences, Peking University, Beijing, China. ³Laboratory for Climate and Ocean–Atmosphere Studies, Department of Atmospheric and Oceanic Sciences, School of Physics, Peking University, Beijing, China. ⁴College of Geosciences, China University of Petroleum (Beijing), Beijing, China. ⁵School of Energy Resources, China University of Geosciences (Beijing), Beijing, China.

✉ e-mail: jinzj1957@pku.edu.cn

records, providing reliable proxies for reconstructing past climates²⁰. However, recent spectral analyses in cyclostratigraphy have frequently demonstrated substantial variations in the clarity and continuity of astronomical signals within sedimentary archives, raising critical questions regarding the factors that control orbital signal stability²¹. Specifically, the processes responsible for obscuring or disrupting these astronomical imprints remain inadequately understood, hindering our ability to interpret sedimentary records confidently and accurately reconstruct past climate dynamics.

Although previous studies have debated the relative impacts of tectonic processes and astronomical forcing on late Paleozoic climate variability^{22–25}, most have assessed these factors in isolation, thereby overlooking their potential interactions and combined influence on climate system dynamics. To address this limitation, we adopt an integrative framework that combines geological datasets with numerical Earth system modeling. Specifically, we incorporate full-plate tectonic reconstructions, geochemical proxies such as strontium isotopes and detrital zircon geochronology, and cyclostratigraphic analyses. These are integrated with climate simulations using the Community Earth System Model (CESM1.2.2) and carbon cycle modeling based on the Long-term Ocean-Atmosphere-Sediment CARbon cycle Reservoir (LOSCAR) model. This combined approach enables a systematic evaluation of how tectonic processes influence the sensitivity of the climate system to astronomical forcing and affect the preservation of orbital signals in sedimentary archives. By explicitly quantifying the interactions between tectonic and orbital controls, our approach offers a distinct perspective on the mechanisms underlying climate state variability and organic carbon burial during one of Earth's most dynamic geological intervals.

Results and Discussion

Tectonic phases in the late Paleozoic

Tectonic activity during the late Paleozoic profoundly impacted Earth's climate system, shaping the geological landscape^{2,13} while simultaneously influencing polar ice sheet dynamics and global sea-level changes^{26,27}. To characterize its temporal evolution, we compiled multiple complementary datasets, including subduction zone and mid-ocean ridge (MOR) lengths, surface production rates ($\text{km}^2 \text{Myr}^{-1}$), global detrital zircon age densities, marine strontium isotopic ratios ($^{87}\text{Sr}/^{86}\text{Sr}$), atmospheric $p\text{CO}_2$ reconstructions, and LOSCAR-based carbon cycle simulations (Fig. 1). These records collectively constrain patterns of lithospheric recycling, continental crustal growth, mantle CO_2 degassing, and their climate feedbacks across the Carboniferous and Permian.

Subduction zone and MOR lengths, together with surface area production rates ($\text{km}^2 \text{Myr}^{-1}$), provide direct constraints on lithospheric recycling, crustal accretion, and the reorganization of plate boundaries¹³. Peaks in global detrital zircon age densities further indicate pulses of continental arc magmatism and crustal addition^{22,28,29}, while troughs reflect tectonic slowdown and reduced magmatic fluxes. $^{87}\text{Sr}/^{86}\text{Sr}$ values provide geochemical insight into the balance between continental weathering and MOR-derived mantle inputs. High $^{87}\text{Sr}/^{86}\text{Sr}$ ratios indicate increased contributions from continental sources, while low ratios are associated with enhanced MOR activity, offering critical insights into the global geochemical cycle and its linkage to tectonic dynamics^{30,31}. Simultaneously, LOSCAR model results capture changes in carbon release magnitude and isotopic composition, offering an integrated perspective on how tectonic outgassing shaped atmospheric $p\text{CO}_2$ levels and carbon isotope trends^{32–34} (Fig. 1a–d). Based on consistent cross-validation among these datasets, three tectonic phases can be recognized during the late Paleozoic, providing a framework for understanding the episodic nature of tectonic processes and their impact on magmatism and geochemical cycles. The intervals are defined as follows: 360–330 Ma (Phase I) and 280–250 Ma (Phase III) represent periods of elevated

tectonic activity, while 330–280 Ma (Phase II) corresponds to a phase of reduced tectonic activity (Fig. 1). These phases are defined by relative changes in tectonic intensity rather than discrete geochronological boundaries, reflecting long-term trends in Earth system behavior.

Phase I (360–330 Ma) is marked by widespread subduction and MOR expansion, with detrital zircon frequencies reaching high values, indicating widespread continental magmatism. $^{87}\text{Sr}/^{86}\text{Sr}$ values trend lower, reflecting greater mantle input from seafloor spreading. In the LOSCAR simulations, this phase is represented by relatively elevated carbon input rates (averaging $-0.041 \text{Pg C yr}^{-1}$; Fig. 1h; Fig. S1), consistent with enhanced volcanic outgassing and active crustal recycling. Phase II (330–280 Ma) is characterized by a pronounced decline in subduction zone and MOR lengths, reduced crustal production rates, and troughs in zircon age distributions (Fig. 1). This interval shows elevated $^{87}\text{Sr}/^{86}\text{Sr}$ ratios, suggesting dominance of continental inputs and diminished MOR influence. In the carbon cycle simulations, this interval is represented by significantly lower carbon input rates (averaging $<0.02 \text{Pg C yr}^{-1}$; Fig. 1h; Fig. S1), resulting in relatively stable or declining $p\text{CO}_2$ concentrations. These factors collectively support an interpretation of this interval as a time of tectonic slowdown, with reduced volcanic degassing. This period was accompanied by the expansion and stabilization of large polar ice sheets, particularly in the Southern Hemisphere³⁵. Phase III (280–250 Ma) marks a renewed phase of elevated tectonic activity. Subduction zone lengths and surface production increase, accompanied by resurgent magmatism recorded in detrital zircon peaks (Fig. 1). Concurrent decreases in $^{87}\text{Sr}/^{86}\text{Sr}$ ratios suggest intensified MOR input, consistent with enhanced mantle-derived strontium fluxes. Carbon input rates rise significantly during this phase in LOSCAR simulations (averaging $-0.063 \text{Pg C yr}^{-1}$; Fig. 1h; Fig. S1), reflecting a shift toward intensified mantle outgassing and large-scale magmatism. This resurgence likely contributed to the retreat of polar ice sheets and more pronounced global sea-level fluctuations^{36,37}. While the precise transitions between phases are inherently gradual and somewhat uncertain, our classification emphasizes the existence of distinct phases defined by robust temporal trends rather than rigid geochronological cutoffs. We acknowledge the simplification involved in applying discrete phase boundaries, yet this framework is effective for identifying first-order relationships among tectonic background, carbon emissions, and climate sensitivity across the late Paleozoic Earth system.

Instability and obscuration of astronomical signals

Sea-level fluctuations offer a sensitive proxy that integrates multiple climate and geological processes operating across various timescales^{12,38,39} (Supplementary Information). On tectonic timescales, processes such as subduction and mid-ocean ridge expansion significantly impact global sea level by redistributing water between Earth's interior and surface reservoirs¹². At shorter, climatic timescales, sea-level variations primarily reflect the cyclic growth and retreat of ice sheets, thermal expansion of seawater, and changes in continental water storage, all of which are closely modulated by astronomical forcing through variations in solar insolation^{40–42}. Therefore, orbital signals preserved in sea-level records represent a valuable means to investigate how tectonic activity might alter the expression and detectability of astronomical climate forcings. Clarifying this interaction is essential, as misinterpreting tectonically influenced sea-level changes solely as orbital signals risks distorting our understanding of past climate behavior and the underlying mechanisms driving global climate variability.

To assess how tectonic background influences the expression of astronomical forcing in sedimentary archives, short-period sea-level cycles across the late Paleozoic were analyzed using multiple lines of evidence. Statistically significant differences in sea-level cycle durations are observed when comparing intervals characterized by

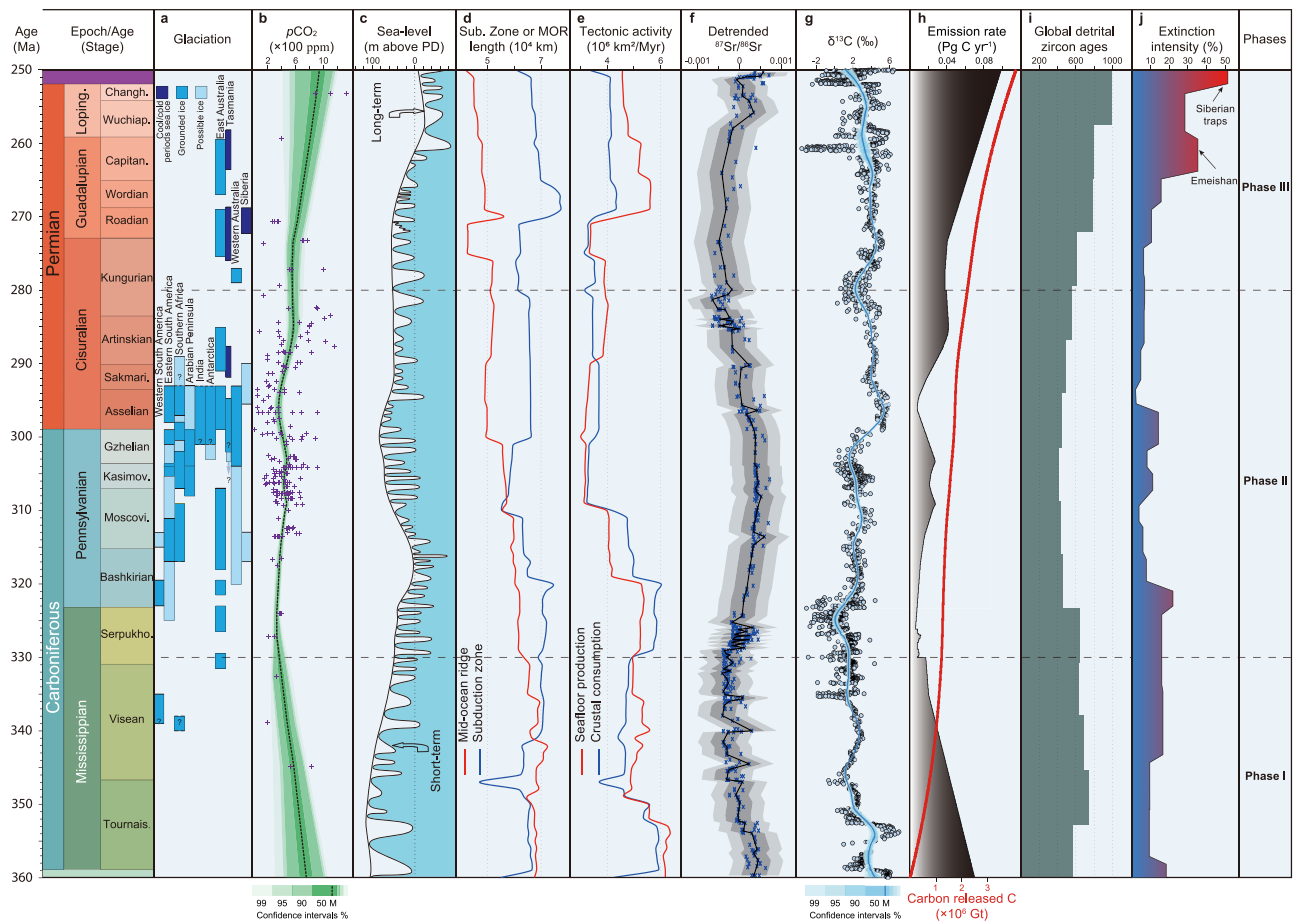


Fig. 1 | Late Paleozoic tectonic activity, climate, and sea-level changes. **a** The glaciation history with grounded ice and possible ice coverage across major regions¹. **b** The partial pressure of atmospheric CO₂ (pCO₂) reconstructions compiled from multiple geochemical proxies (purple crosses)^{9,71,91} with a 35% locally weighted scatterplot smoothing (LOWESS) trend line. **c** Long-term and short-term sea-level changes relative to present-day levels⁸⁵. **d** Lengths of mid-ocean ridge (MOR) and subduction zones¹³. **e** The intensity of plate tectonic activity through subduction and MOR dynamics¹³. **f** ⁸⁷Sr/⁸⁶Sr isotope ratios after removing a long-term trend⁹². **g** Carbon isotope composition (δ¹³C) values from marine sedimentary

carbonates⁸¹ with a 15% locally estimated scatterplot smoothing (LOESS) trend line, compiled from regionally variable sources for the Carboniferous and predominantly from early Permian datasets⁹³, representing a first-order approximation of long-term isotopic trends. **h** Modeled carbon emission rates (black area) and cumulative carbon release (red curve) derived from LOSCAR (Long-term Ocean-Atmosphere-Sediment Carbon cycle Reservoir) simulation. **i** Frequency histograms of global detrital zircon age counts²². **j** Extinction intensity across the late Paleozoic⁹². Phases I, II, and III denote tectonic phases defined in this study, corresponding to -360–330 Ma, -330–280 Ma, and -280–250 Ma, respectively.

reduced tectonic activity (Phase II; -330–280 Ma) with those exhibiting elevated tectonic activity (Phases I and III; -360–330 and -280–250 Ma) (Fig. 2; Fig. S3). To assess whether the observed cyclicities reflect periodicities consistent with astronomical control, circular spectral analysis (CSA) was performed on both sea-level cycle and sequence duration datasets. These results reveal that cyclicities within the range of 0.5–2.0 Myr are statistically significant during intervals of reduced tectonic activity, whereas signal coherence diminishes under more tectonically active conditions (Fig. 2; Fig. S3). Besides, during intervals of reduced tectonic activity (Phase II; -330–280 Ma), sea-level cycles were consistently shorter and more tightly clustered (mean = 1.44 ± 0.61 Myr, *n* = 38). In contrast, periods of elevated tectonic activity (Phases I and III; -360–330 Ma and -280–250 Ma) were associated with longer and more dispersed cycle durations (mean = 1.85 ± 1.00 Myr, *n* = 31) (Fig. 2a). These differences are statistically robust, supported by Welch's *t*-test (*t* = -4.44, *p* = 0.0001), *F*-test (*F* = 6.85, *p* < 0.0001), and one-way ANOVA (*F* = 23.03, *p* < 0.0001) (Supplementary Data 3). A similar pattern is also evident in the sequence stratigraphic records (Fig. S3; Supplementary Data 3).

Several plausible mechanisms may account for the observed differences in sea-level cycle durations and variabilities. Most notably, during tectonically reduced intervals, sedimentary basins likely

experienced more stable accommodation space, lower sedimentation variability, and reduced environmental noise, facilitating clearer astronomical pacing. In contrast, elevated tectonic activity may have disrupted signal fidelity through enhanced basin subsidence, variable sediment supply, and localized deformation⁴³ (Figs. 2, S3). These alterations might modify the boundary conditions of the climate system, thereby reducing its sensitivity to orbital forcing and diminishing the fidelity of preserved orbital signals¹⁹. Second, variations in long-term orbital modulation cycles or chaotic behavior within the solar system could potentially introduce uncertainties into sedimentary records⁴⁴, although clear evidence supporting this hypothesis remains limited during the late Paleozoic. Lastly, biases and chronological uncertainties inherent in sea-level reconstructions might introduce variability; however, sensitivity analyses and multi-region cross-validation largely mitigate this possibility (Fig. S2). Although multiple mechanisms warrant consideration, the impact of varying tectonic intensity on the stability of orbital signals remains one of the most strongly supported explanations.

Late Paleozoic climate state variability

Climate variability, defined as the degree of fluctuation in climate variables such as temperature and precipitation, profoundly influences

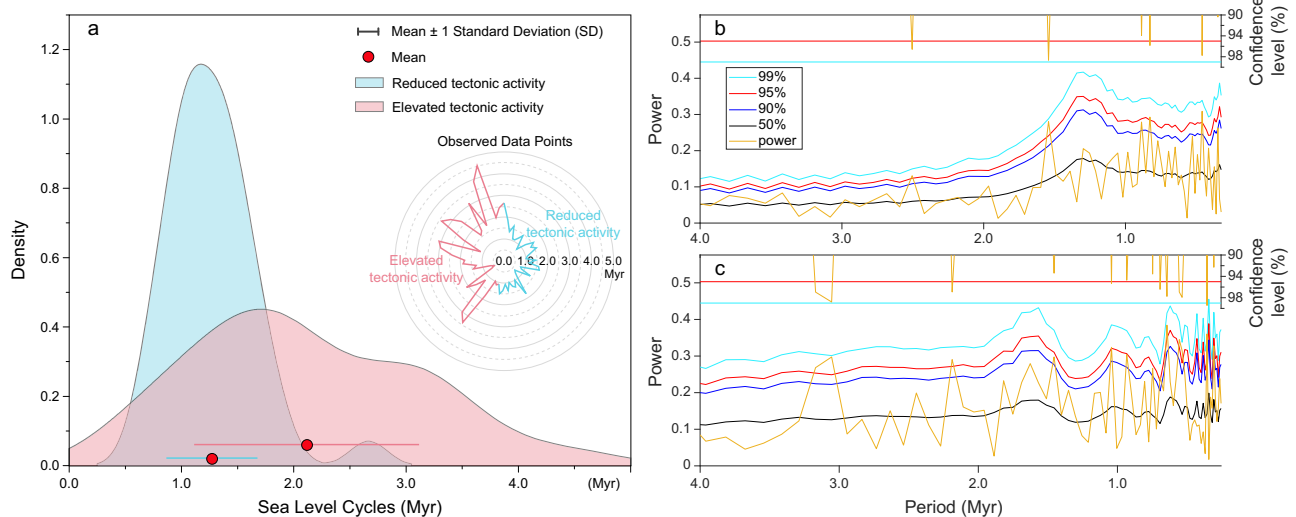


Fig. 2 | Sea-level cycle frequency and duration during periods of reduced and elevated tectonic activity. **a** Kernel density estimates of sea-level cycle durations (Myr) under two tectonic regimes: reduced tectonic activity (blue) and elevated tectonic activity (pink), corresponding to Phases II and Phases I + III, respectively. Red dots and horizontal bars denote the mean \pm 1 standard deviation for each

group. Inset rose diagram illustrates the distribution and concentration of cycle durations in circular space. **b** Circular spectral analysis (CSA) results of sea-level cycles during periods of reduced tectonic activity. Power spectrum (gold line) is plotted alongside Monte Carlo-derived confidence levels. **c** CSA results for sea-level cycles during elevated tectonic activity.

biological habitats, resource availability, and ecosystem stability^{45,46}. To assess the relative contributions of continental configuration, orbital parameters, and atmospheric CO₂ concentrations to climate state variability, targeted sensitivity experiments were conducted using CESM for three representative time slices: 340 Ma, 300 Ma, and 260 Ma (Fig. 3). These intervals span the entire duration of our study and capture contrasting tectonic and climatic regimes. The results indicate that variations in paleogeographic boundary conditions alone account for only minor differences in the spatial and temporal structure of climate variability (Fig. 3). In contrast, simulations with elevated atmospheric CO₂ levels yield substantially greater variability in GMST and GMP (Fig. 4). These findings are consistent with the well-established principle that warmer climate systems exhibit heightened sensitivity to both internal variability and external forcings^{47,48}. Therefore, the pronounced increase in variability during Phases I and III was likely primarily driven by elevated atmospheric CO₂ concentrations (Figs. 4, S5–S8). Elevated atmospheric CO₂ levels during Phases I and III likely arose predominantly from intensified tectonic degassing associated with enhanced subduction and volcanic activity (Fig. 1). Additionally, secondary mechanisms such as increased silicate weathering^{49,50} (which removes CO₂ through chemical reactions) and reduced efficiency of organic carbon burial (which limits long-term carbon storage; Fig. 6) may further modulate atmospheric CO₂ concentrations. However, a notable exception arises at 250 Ma, where elevated CO₂ levels are paradoxically associated with a slight decrease in GMST and GMP (Fig. 4). A similar pattern has been observed in other modeling studies of the earliest Mesozoic, where reduced climate variability is reported around 250 Ma despite high atmospheric CO₂ levels⁵¹. We hypothesize that this anomaly reflects the unique paleogeographic context of that time. Unlike earlier periods, the paleogeographic reconstruction for 250 Ma reveals nearly complete assembly of Pangaea and the closure of low-latitude seaways in the Tethys domain. These changes likely disrupted equatorial heat and moisture transport pathways^{52,53}, thereby dampening the expected amplification of climate variability under high-CO₂ conditions.

Atmospheric CO₂ appears to play a central role in amplifying the climate system's sensitivity to astronomical forcing. As demonstrated by the sensitivity experiments (Fig. 3), elevated *p*CO₂ levels markedly increase GMST variability under a range of orbital configurations.

Spatial patterns at 300 Ma (Fig. 5) further show that the differences in surface temperature and precipitation between high and low eccentricity–obliquity scenarios are significantly enhanced under elevated *p*CO₂. These results indicate that elevated atmospheric CO₂ intensifies radiative forcing and concurrently enhances the climate system's sensitivity to insolation variability driven by orbital parameters. This enhanced sensitivity may be mediated by threshold behaviors and nonlinear feedbacks^{54,55}, including abrupt glacial–interglacial transitions driven by ice volume sensitivity and ocean circulation reorganizations that modulate nutrient supply and biological productivity. Therefore, the observed climate instability during Phases I and III may mainly reflect a coupled response to rising atmospheric CO₂ concentrations and orbital-scale insolation variability.

Organic carbon enrichment during icehouse period

Our synthesis of late Paleozoic organic-rich shale and coal deposits (Fig. 6) reveals a pronounced increase in deposition frequency during Phase II (~330–280 Ma), an interval characterized by relatively reduced tectonic activity compared to the preceding and following stages of intensified tectonism. Both volcanic activity and astronomical forcing are commonly identified as two crucial factors that influence organic matter accumulation^{56,57}. Volcanic activity influences organic carbon dynamics through complex and bidirectional mechanisms. Moderate volcanism enhances nutrient availability by promoting silicate weathering and supplying trace elements such as phosphorus and iron, which together stimulate marine primary productivity^{50,58}. In contrast, excessive volcanic episodes can perturb the climate system across multiple timescales. While short-lived eruptions may trigger transient cooling through stratospheric sulfate aerosol formation, particularly in the context of large igneous province volcanism, prolonged CO₂ outgassing leads to sustained warming and environmental stress^{59,60}. Over multimillion-year timescales, volcanism thus serves as a major source of greenhouse gases, reducing the preservation potential of organic matter through climatic destabilization⁶¹. Given that multiple geological indicators and carbon cycle model results suggest a substantial decline in volcanic activity during Phase II compared to Phases I and III (Figs. 1, S1). Such subdued volcanic conditions may have acted to enhance nutrient availability and primary productivity without

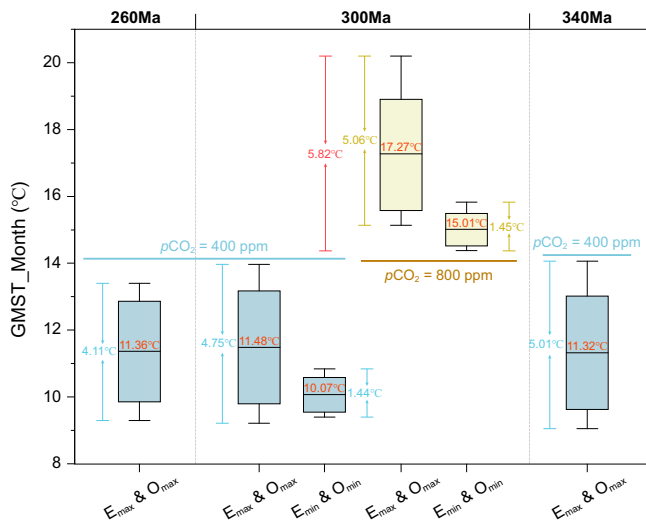


Fig. 3 | Sensitivity of GMST variability to orbital forcing and atmospheric $p\text{CO}_2$ at selected late Paleozoic time slices. Box plots show monthly global mean surface temperature (GMST, °C) simulated under different combinations of orbital configurations and atmospheric CO_2 concentrations for 260 Ma, 300 Ma, and 340 Ma. At 260 Ma and 340 Ma, simulations were conducted under maximum orbital eccentricity and obliquity (E_{max} & O_{max} ; eccentricity = 0.066, obliquity = 24.5°) with atmospheric $p\text{CO}_2$ fixed at 400 ppm. At 300 Ma, four scenarios were tested: (1) E_{max} & O_{max} at 400 ppm CO_2 (light blue), (2) E_{max} & O_{max} at 800 ppm CO_2 (khaki), (3) E_{min} & O_{min} at 800 ppm CO_2 (khaki; eccentricity = 0, obliquity = 22.5°), and (4) E_{min} & O_{min} at 400 ppm CO_2 (light blue). Boxes represent the interquartile range (25th–75th percentile), red lines denote the mean GMST, and whiskers span the full range from minimum to maximum monthly values. Annotated arrows indicate the spread of monthly GMST variability under each scenario.

triggering climate instability, thereby contributing positively to the observed organic matter enrichment. Astronomical forcing, in contrast, modulates climate variability by regulating seasonal and latitudinal patterns of solar insolation, thereby influencing temperature, precipitation, and hydrological cycling^{18,62}. While the fundamental frequencies of orbital parameters are set by planetary mechanics and evolve on predictable timescales^{17,23}, their climatic expression is strongly modulated by boundary conditions, including atmospheric CO_2 levels, ice volume, and tectonic configurations (Figs. 3–5). Consequently, the climatic and depositional imprint of orbital cycles can vary substantially across geologic intervals. The observed increase in organic-rich sedimentation during Phase II, coupled with evidence of more coherent astronomical cyclicity during this interval (Fig. 2), suggests that reduced tectonic disturbance may have facilitated the clear imprint of astronomical forcing in sedimentary systems.

We propose that comparatively reduced tectonic activity, in combination with low climate variability, played a key role in promoting organic matter accumulation during the late Paleozoic. Unlike the more geodynamically active intervals, Phase II (~330–280 Ma) coincided with an icehouse regime characterized by relatively low atmospheric CO_2 levels, reduced climate variability in model simulations, and a more coherent expression of astronomical forcing (Figs. 3, 4). The cyclic patterns in sea-level variability and depositional architecture during this phase are commonly interpreted to reflect orbitally paced fluctuations in continental glacier volume and continental water storage^{42,63}. Under reduced tectonic forcing, diminished crustal disturbance and enhanced accommodation continuity likely facilitated the preservation of such sedimentary rhythms, thereby improving the fidelity of astronomical signal expression in stratigraphic archives^{64–66} (Fig. 7a). This climatic backdrop created favorable conditions for biological productivity and rhythmic organic matter

deposition, which facilitated the widespread development of organic-rich shales and coal beds in several regions, including North America, Europe, South China, and North China, sustaining an organic-rich icehouse period (Fig. 6b). Additionally, the spatial distribution of organic-rich shales and coals during this phase was predominantly concentrated between paleo-latitudes of 0° to 40°, although several occurrences are also observed between 40°S and 60°S (Fig. 6b). This pattern suggests that warm and humid equatorial to mid-latitude conditions facilitated both high productivity and effective preservation under relatively stable depositional settings. Within this framework, astronomical forcing likely paced climate fluctuations, further reinforcing the cyclic nature of organic carbon burial^{54,67}. Collectively, the coupling of low-frequency climatic variability with enhanced orbital pacing provided optimal conditions for sustained organic matter accumulation during this critical interval.

Elevated climate variability associated with periods of intensified tectonic forcing (Fig. 4), involving frequent fluctuations in temperature and precipitation, likely exerted substantial ecological stress through multiple interconnected pathways. Pronounced temperature fluctuations could periodically shorten or disrupt plant growing seasons, suppressing net primary productivity and consequently reducing the efficiency of terrestrial carbon sequestration capacity^{68,69}. Similarly, greater precipitation variability likely amplified hydrological extremes (e.g., floods and droughts) during specific intervals. These extremes could further disturb sedimentary environments via abrupt sediment transport or erosion and impose long-term ecological stress, including nutrient loss and reduced resilience of biological communities to environmental fluctuations⁷⁰. These environmental stressors did not universally suppress ecosystem productivity, as shown by flourishing ecosystems during certain warm intervals of the Cretaceous. In contrast, the late Paleozoic, characterized by extensive glaciation and large ice-volume variability¹, ecosystems appear to have been more vulnerable to rapid environmental shifts⁷¹.

Further, intensified tectonic processes such as major volcanism, widespread mid-ocean ridge expansion, and continental orogeny during active intervals significantly modified Earth's surface topography and ocean circulation patterns (Fig. 7b). These large-scale perturbations likely increased the variability and instability of regional climate systems, particularly through enhanced fluctuations in temperature and precipitation (Fig. 4). Such conditions may have impaired the recording and preservation of astronomical signals in sedimentary archives, as demonstrated by the broader and more irregular distribution of sea-level cycle durations during periods of elevated tectonic activity (Fig. 2; Fig. S3). A reduced number and fragmented distribution of organic-rich shales and coals observed during these intervals (Fig. 6) suggest significant disruptions to sedimentary continuity, consistent with increased depositional environmental instability caused by tectonic disturbances. These lines of evidence indicate that tectonic-driven environmental instability likely posed substantial challenges to ecosystems and sedimentary processes, ultimately limiting organic matter accumulation.

These results reveal the pivotal influence of tectonic conditions on how the climate system responded to astronomical forcing during the late Paleozoic. Intervals of reduced tectonic activity appear to have provided a relatively stable climatic background that facilitated coherent orbital pacing, enhanced biological productivity, and promoted widespread burial of organic matter in the form of shales and coals. In contrast, during intervals of elevated tectonic activity, the Earth system likely responded to astronomical forcing in more variable and nonlinear ways, amplifying climatic oscillations and disrupting depositional continuity. Notably, this variability does not imply instability in the orbital parameters themselves; instead, it reflects the dynamic response of the Earth system to external forcing under varying tectonic regimes (Fig. 7). While this study focuses on physical drivers of climate and carbon cycle interactions, the evolution of

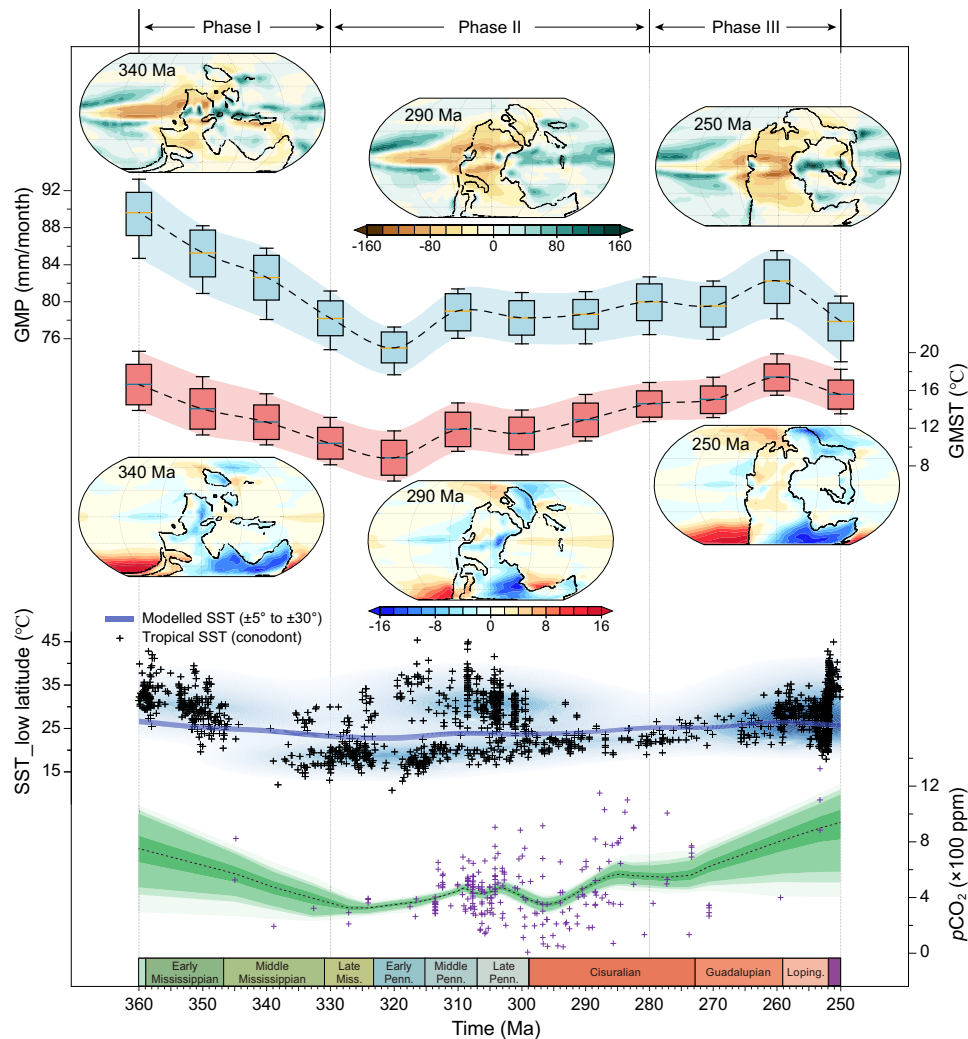


Fig. 4 | Late Paleozoic climate variability in temperature and precipitation (360–250 Ma). The temporal evolution of global mean surface temperature (GMST, °C) and global mean precipitation (GMP, mm/month) variability during the late Paleozoic (360–250 Ma) is derived from a suite of fully coupled Community Earth System Model (CESM) simulations conducted at 10-million-year intervals across 12 time slices. The red shaded area with box plots represents monthly variability in global mean surface temperature, while the blue shaded area with box plots corresponds to monthly variability in global mean precipitation. The dashed lines denote the mean values for each period, and the boxes indicate the inter-quartile range (25–75%). Six additional inset maps show zonal surface temperature

differences and zonal precipitation differences for the time points 340 Ma, 290 Ma, and 250 Ma. CESM-simulated SST (sea surface temperature) averaged over paleolatitudes of $\pm 5^\circ$ and $\pm 30^\circ$ define the upper and lower bounds of the shaded band (dark blue), representing tropical SST variability across time. Conodont-based SST reconstructions (black crosses) are compiled from equatorial regions corresponding to paleolatitudes within the tropical belt, and the probability density distribution is visualized as a light blue background. The modeled SST consistently align with the empirical range, supporting the validity of CESM temperature outputs⁹⁴. At the base, atmospheric $p\text{CO}_2$ estimates and LOWESS trendline as in Fig. 1b.

terrestrial vegetation likely also influenced organic carbon burial⁷². Changes in plant diversity and productivity, such as the expansion of seed plants and the collapse of tropical rainforests, may have affected carbon sequestration by altering biomass, soil formation, and sediment transport^{73,74}. Although not included in the present modeling framework, such vegetation feedbacks are relevant to the broader Earth system and merit integration in future coupled simulations. Together with tectonic forcing, these biotic processes likely shaped how the climate system responded to astronomical variations. Recognizing this interaction provides a framework for interpreting carbon burial patterns in deep-time archives and offers useful analogs for other icehouse intervals.

Methods

Climate model experiments

Late Paleozoic climate dynamics (360–250 Ma) were investigated using the Community Earth System Model (CESM1.2.2), a fully coupled

Earth system model incorporating atmosphere, ocean, land, and sea ice components⁷⁵. The atmospheric and land components use the Community Atmosphere Model version 4 (CAM4) and Community Land Model version 4 (CLM4), respectively^{76,77}, both configured with a horizontal resolution of $3.75^\circ \times 3.75^\circ$ (T31 grid). The ocean (POP2) and sea ice (CICE4) components operate on a nominal 3° horizontal grid (g37), with 60 and 26 vertical layers, respectively^{78,79}. Twelve simulations were conducted, each representing a 10-million-year time slice spanning from 360 Ma to 250 Ma (Fig. S4; Supplementary Data 4). Each run was initialized using reconstructed paleogeography consistent with the corresponding time interval. All other greenhouse gases, orbital parameters, and aerosol properties were held constant. Orbital parameters were fixed to a maximum eccentricity scenario (eccentricity = 0.066, obliquity = 24.5° , longitude of perihelion = 90°) to ensure consistent astronomical forcing across time slices. Each simulation was integrated for a minimum of 2000 years, and the final 100 years were used for analysis only after equilibrium was reached,

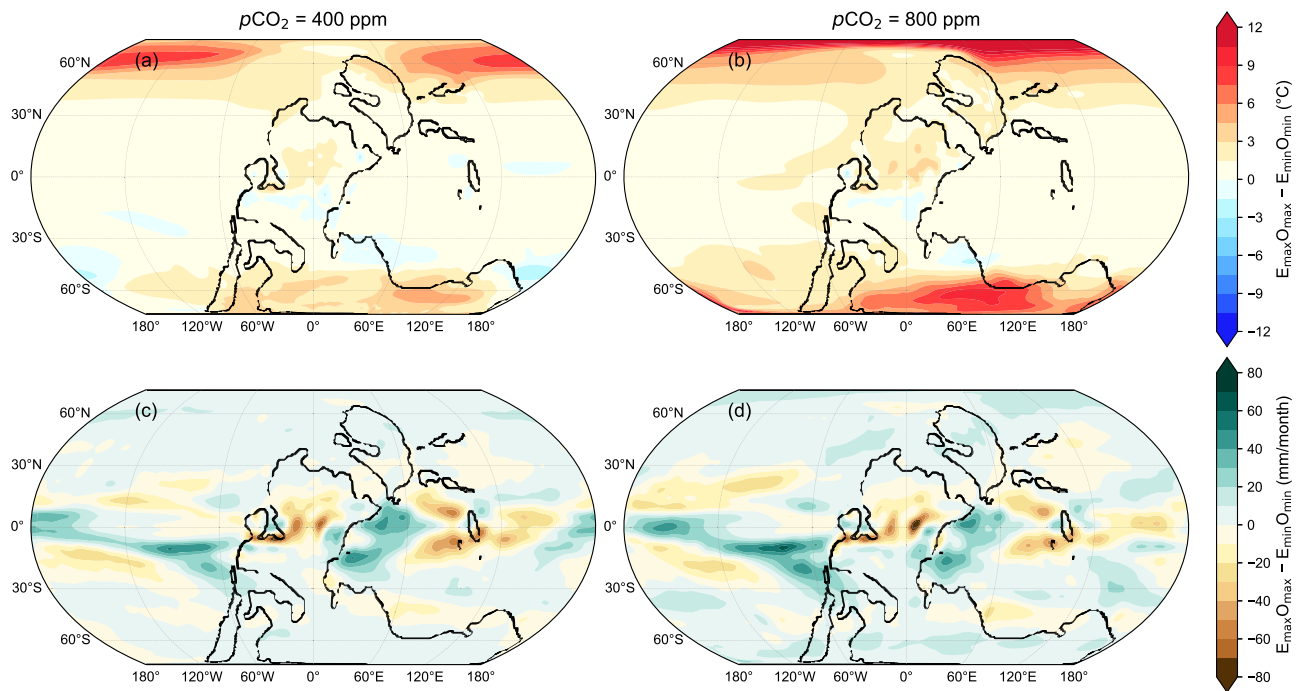


Fig. 5 | Spatial differences in temperature and precipitation driven by orbital forcing under varying atmospheric $p\text{CO}_2$ levels at 300 Ma. Maps illustrate the climatic response to different orbital configurations (E_{max} & O_{max} versus E_{min} & O_{min}) at 300 Ma, evaluated under atmospheric CO_2 concentrations of 400 ppm and

800 ppm. **a, b** Annual mean surface temperature differences ($^{\circ}\text{C}$) between E_{max} & O_{max} and E_{min} & O_{min} configurations. **c, d** Monthly mean precipitation differences (mm/month) under the same configurations.

defined by a global net top-of-atmosphere (TOA) radiative flux below 0.1 W m^{-2} (Fig. S4)⁸⁰. These simulations reveal broadly consistent climate patterns across the Carboniferous and Permian. Surface temperatures and precipitation are highest near the equator and in tropical regions, whereas high-latitude zones remain cold and relatively dry (Fig. S5, S6).

In addition to the 12 baseline simulations, a series of targeted sensitivity experiments was conducted to examine the combined effects of orbital forcing and atmospheric CO_2 concentrations (Fig. S4; Supplementary Data 4). At 260 Ma and 340 Ma, two simulations were performed under maximum eccentricity and obliquity conditions (eccentricity = 0.066; obliquity = 24.5°), with atmospheric $p\text{CO}_2$ fixed at 400 ppm. At 300 Ma, four simulations tested the combined effects of orbital geometry and CO_2 levels: (1) E_{max} & O_{max} at 400 ppm $p\text{CO}_2$, (2) E_{max} & O_{max} at 800 ppm $p\text{CO}_2$, (3) E_{min} & O_{min} at 800 ppm $p\text{CO}_2$ (eccentricity = 0; obliquity = 22.5°), and (4) E_{min} & O_{min} at 400 ppm $p\text{CO}_2$. These experiments provide critical insights into how orbital variability and CO_2 radiative forcing jointly influence GMST variability and precipitation responses at orbital time scales (Figs. 3, 5).

LOSCAR carbon cycle model

Long-term carbon cycle dynamics during the Late Paleozoic were simulated using the LOSCAR (Long-term Ocean-Atmosphere-Sediment Carbon cycle Reservoir) model. LOSCAR is a box-model framework designed to capture the partitioning of carbon among the atmosphere, ocean, and sediments over long timescales, while explicitly tracking $\delta^{13}\text{C}$ evolution in the surface ocean and atmospheric $p\text{CO}_2$ levels^{32–34}. The model consists of coupled modules representing ocean circulation, atmospheric exchange, biological productivity, weathering, and sedimentation³². In this simulation, LOSCAR includes 10 ocean boxes, subdivided into surface, intermediate, and deep layers for three major paleo-ocean domains and a high-latitude reservoir. All surface boxes are coupled to a single atmospheric box, enabling simulation of air-sea carbon exchange.

In the original LOSCAR design, emission forcing files contain only two columns: time and the carbon emission rate (Pg C yr^{-1}). This format requires segmenting longer time-series runs whenever the carbon isotopic composition ($\delta^{13}\text{C}$) of emissions needs to vary through time. For studies involving geologically realistic, continuous changes in both emission rates and isotopic composition, particularly relevant to the late Paleozoic, this rigid structure constrains model flexibility and reduces computational efficiency. To improve input flexibility, we introduced a structural modification to the model input format, enabling the revised LOSCAR version to accept a three-column emission file specifying: (1) time (yr), (2) carbon emission flux (Pg C yr^{-1}), and (3) $\delta^{13}\text{C}$ of emitted carbon (‰). The model now directly integrates variable isotopic trajectories, eliminating the need to manually segment emission events into artificial steps with constant $\delta^{13}\text{C}$, which was previously necessary for long-duration, high-resolution simulations. The revised structure allows the model to continuously ingest time-resolved changes in both flux and isotopic composition from a single control file, improving simulation fidelity under geologically complex boundary conditions.

To adapt the LOSCAR model to the late Paleozoic interval, key initial parameters were revised to align with boundary conditions constrained by global geochemical and climate reconstructions (Supplementary Data 1). The initial global surface ocean dissolved inorganic carbon (DIC) $\delta^{13}\text{C}$ was adjusted to 3.5‰, approximating observed late Paleozoic carbonate records⁸¹. The emitted arc volcanic CO_2 is assumed to have $\delta^{13}\text{C} = -3\text{‰}$ ⁸². The modeled $\delta^{13}\text{C}$ signal was derived by calculating the area-weighted mean $\delta^{13}\text{C}$ across all surface ocean boxes, thereby integrating spatial heterogeneity while retaining consistency with marine carbonate proxy data. The final steady-state atmospheric CO_2 concentration was set to 750 ppm to match geological CO_2 proxy constraints and ensure mass balance in the silicate weathering–degassing cycle. Climate sensitivity was activated by enabling temperature feedbacks (TSNS = 1), and the climate response to CO_2 doubling was set at 4.6°C . All other physical and

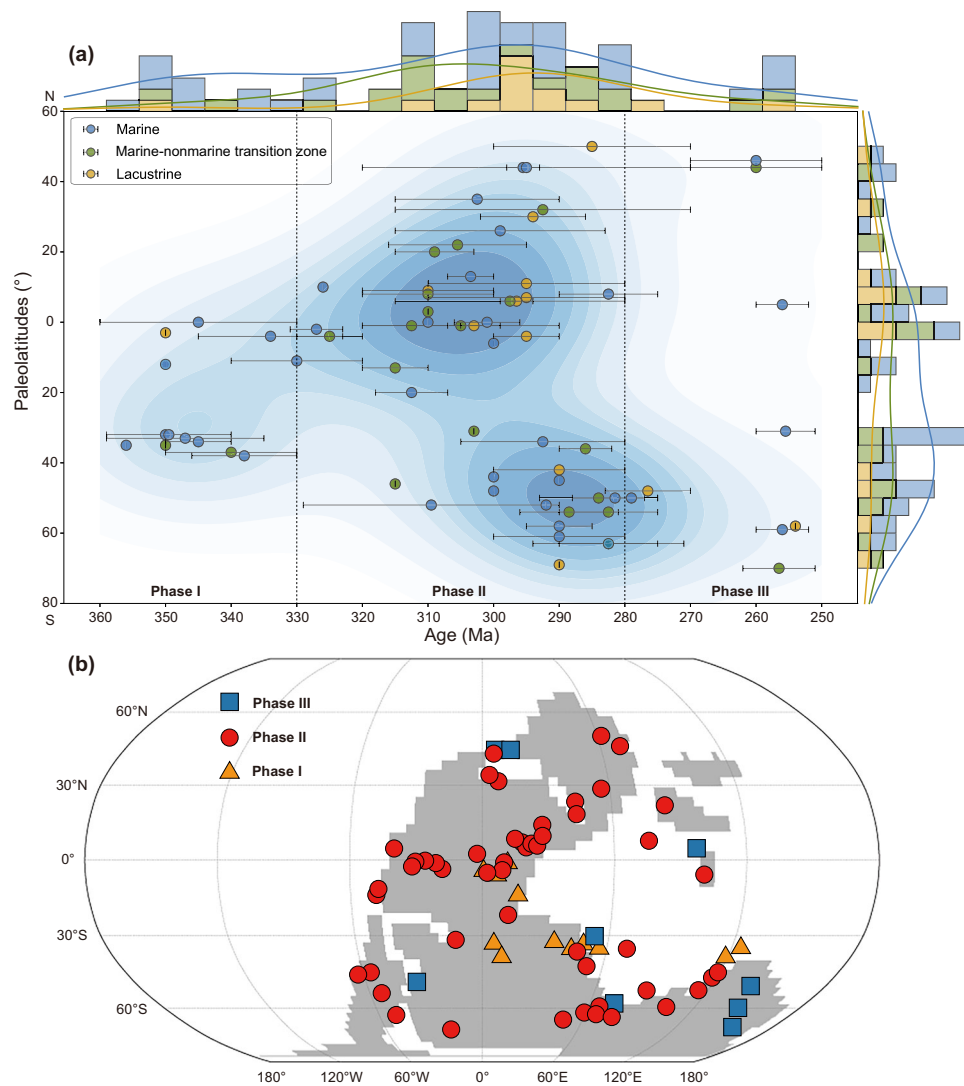


Fig. 6 | Spatial and temporal distribution of organic-rich shales and coals during the late Paleozoic. a The distribution of organic-rich shales and coals across different paleolatitudes and time periods during the late Paleozoic. Each point represents a deposit from a marine, marginal, or lacustrine environment, with the color-coded dots corresponding to different depositional environments: blue for marine, green for MNT (Marine-nonmarine transition zone), and orange for lacustrine. Horizontal bars indicate age uncertainty associated with each deposit. The top histogram shows the frequency of organic-rich sediment deposition over

time, while the side histogram shows their distribution by paleolatitude. The denser accumulation of deposits in tropical to subtropical regions (0° to 40° paleolatitude) is evident, especially during tectonically relatively stable periods such as Phase II. **b** The spatial distribution of organic-rich shales and coals during different tectonic phases. The majority of organic-rich deposits during Phase II are located in tropical and subtropical latitudes, with a relatively high density compared to the more broadly distributed records in Phases I and III (See Fig. S9 for details).

geochemical parameters (e.g., deep ocean temperature, biological pump efficiency, shelf-basin rain ratio) were maintained at either CESM-derived or default LOSCAR values, unless otherwise noted in Supplementary Data 1. The prescribed $\delta^{13}\text{C}$ trajectory used in the emission input file was directly extracted from the global carbonate compilation presented in GTS2020⁸¹. While this dataset integrates data from diverse depositional settings, including shallow-water carbonate platforms with potential subaerial exposure, it remains one of the few continuous $\delta^{13}\text{C}$ records spanning the entire late Paleozoic interval. Despite possible biases during specific intervals such as the Carboniferous–Permian boundary, its temporal continuity and broad global scope make it suitable for long-term carbon cycle modeling.

Model execution follows a two-stage approach. First, a spin-up simulation under zero-emission conditions was performed for 2 Myr to ensure steady state (global net flux $<10^{-3}$ Pg C yr⁻¹). The resulting

system state (LPIA_ini.dat) served as the baseline for all subsequent emission scenario simulations. Simulations were initiated using control files (e.g., whole.inp) that specified the desired time-varying emission fluxes and isotopic compositions through the modified three-column emission file. The results of the model runs are publicly available on Zenodo⁸³. The objective of this modeling framework is to investigate relative trends in the Earth's carbon cycle under tectonically- and orbitally-modulated forcing, rather than reproducing exact absolute values of each geochemical proxy. As such, minor discrepancies in ocean salinity, temperature distribution, and box boundary interactions, all of which are held constant in the model, are not expected to significantly influence the long-term trajectories of carbon isotope or atmospheric CO₂ evolution. This approach enables robust, comparative analysis of carbon perturbation dynamics across varying tectonic and climatic states during the late Paleozoic.

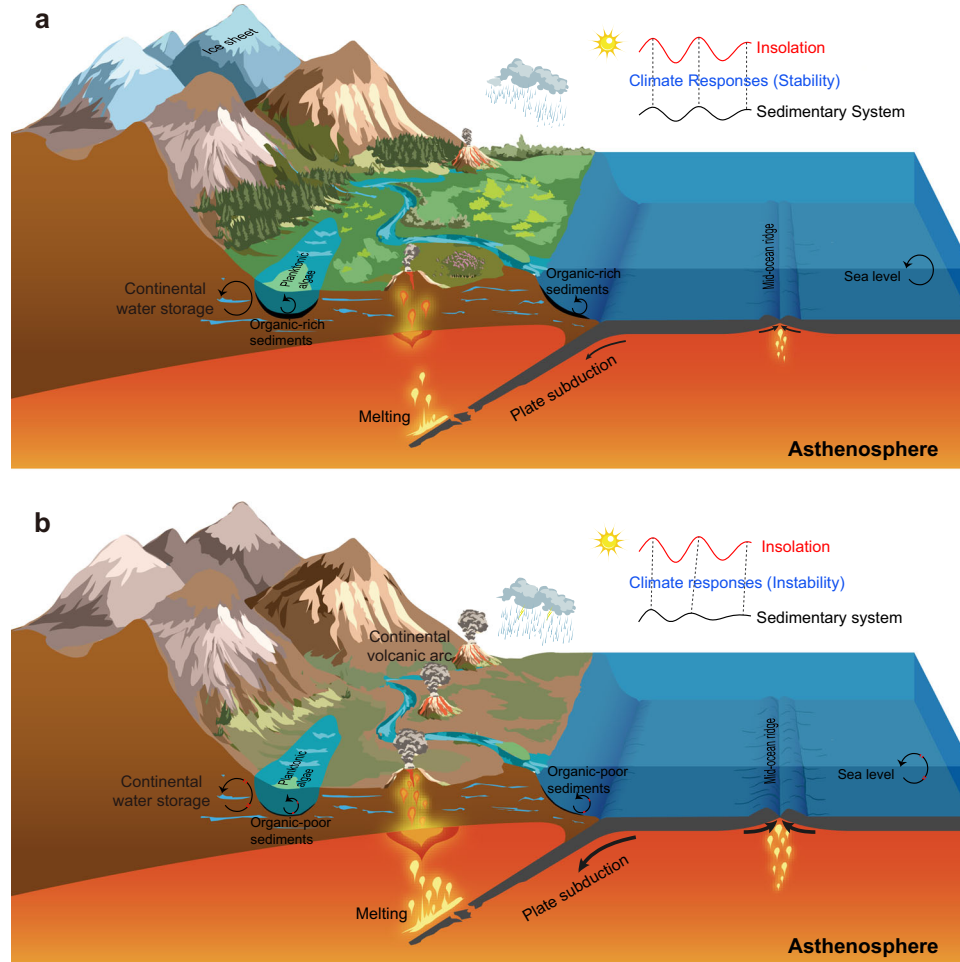


Fig. 7 | Schematic representation of tectonic and climatic influences on organic carbon burial. **a** During intervals characterized by lower tectonic intensity, relatively stable depositional settings and modest volcanic input may enhance the expression of orbital signals in sedimentary archives. These conditions support high biological productivity and promote the rhythmic accumulation and preservation of organic-rich sediments. **b** In contrast, intervals with elevated tectonic

intensity are associated with increased subduction, mid-ocean ridge activity, and continental volcanism. These factors may amplify climate variability and disturb sedimentary environments through enhanced topographic reorganization, fluctuating nutrient fluxes, and altered hydrological regimes. These disruptions reduce biological productivity and the capacity for organic matter burial, leading to less organic-rich sediment accumulation.

Data compilation

The data used in this study were compiled from a comprehensive review of existing literature and stratigraphic records to inform the late Paleozoic climate state, organic matter burial patterns, and tectonic settings. The primary dataset includes organic-rich shale, coal, and lacustrine deposits from various basins around the world, spanning critical time intervals from the Early Carboniferous to the late Permian (360–250 Ma). This dataset is detailed in Supplementary Data 5, which categorizes the formations according to their paleolatitudinal positions, geological settings, and lithologies. These data provide key insights into how organic matter burial was distributed geographically and temporally during different phases of tectonic stability and activity. In this study, paleolatitudinal positions were derived from established paleogeographic reconstructions, and refined using the GPlates platform for paleolatitude recovery^{13,84}.

Specifically, the formations and locations presented in the Supplementary Data 5 were selected based on the presence of organic-rich shales, coals, and lacustrine sediments across marine, transitional, and terrestrial environments. Data sources were compiled from peer-reviewed articles, including stratigraphic studies, paleogeographic reconstructions, and lithological analyses. These data informed the reconstruction of organic matter burial patterns, offering critical

insights into how organic carbon accumulation coincided with periods of tectonic stability (Phase II, 330–280 Ma) and tectonic activity (Phases I and III, 360–330 Ma and 280–250 Ma, respectively). To ensure the reliability of the sea-level dataset, strict selection criteria were applied, including biostratigraphic constraints and lithological validation. Only formations with well-constrained radiometric dating or robust biostratigraphic correlations were included. Each entry was cross-referenced with lithological descriptions to confirm the presence of organic-rich strata, particularly focusing on shale, coal, and lacustrine deposits known for significant organic matter content.

Sea-level analysis and periodicity detection

To evaluate the existence of periodic signals in late Paleozoic sea-level variations, we combined classical peak-interval estimation with circular spectral analysis (CSA) and statistical variance testing. Our primary sea-level dataset is based on the widely adopted global eustatic curve developed by Haq and Schutter (2008), which provides biostratigraphically constrained sea-level fluctuations throughout the Carboniferous and Permian⁸⁵. Although interpretive in nature, this curve remains the most widely used reference for multimillion-year-scale eustatic variations during the Carboniferous and Permian^{86,87}. Temporal resolution and robustness were enhanced by supplementing

the global sea-level curve with high-resolution regional stratigraphic sequences from the Tethyan domain and Donets Basin (Figs. S2, S3).

Short-period sea-level cycles were identified by calculating the time intervals between successive peaks in the detrended sea-level curve, as well as intersections between long-term and short-term components (Fig. 1c). This approach was also applied to the regional sequence datasets. The uncertainty introduced by manual identification of peaks and crossing points is negligible compared to the inherent resolution of the stratigraphic records. To statistically test for the presence of cyclicity in these discrete event sequences, CSA was applied to detect underlying periodic structures in event-based time series without requiring amplitude modulation⁸⁸. CSA has been successfully used in analyzing periodicities in mass extinction events, impact craters, and other episodic geologic phenomena⁸⁹. In this study, CSA was implemented using the *Acycle* 2.8 software⁹⁰, which enables event-based Rayleigh power spectral analysis with Monte Carlo-based significance testing. The analysis was independently performed for short-period sea-level events associated with each tectonic phase. Statistically significant periodicities were identified by comparing Rayleigh power spectra against null distributions generated through stochastic simulations. Importantly, the analysis does not rely on the absolute amplitude or strict synchronicity of sea-level fluctuations, which are susceptible to local tectonics, basin subsidence, or glacio-eustatic coupling. Instead, we focus on the statistical distribution of cycle durations, which are less sensitive to absolute age calibration and better reflect the imprint of astronomical forcing under different tectonic regimes.

In parallel with spectral analysis, sea-level cycle duration distributions were statistically compared across different tectonic regimes to evaluate the impact of tectonic conditions on astronomical signal expression. The data were categorized into intervals of reduced and elevated tectonic activity (Supplementary Data 2). Distributions were tested using Welch's t-test, F-test, and one-way ANOVA (Supplementary Data 3), and visualized through kernel density estimation and violin plots (Fig. 2a). This multi-method approach enabled us to detect orbitally paced signals and quantitatively assess how tectonic activity modulated the expression and preservation of astronomical forcing in sedimentary sea-level records.

Data availability

All datasets generated and analyzed in this study are publicly archived on Zenodo at <https://doi.org/10.5281/zenodo.15645982>⁸³. The repository includes outputs from climate simulations using CESM1.2.2 and carbon cycle simulations using the LOSCAR model. In addition, Supplementary Data 1–5 are archived in a separate supplementary file provided with this article.

Code availability

The codes used in this study are publicly archived on Zenodo at <https://doi.org/10.5281/zenodo.15645982>. These include Python scripts used to generate selected figures in the main text and Supplementary Information.

References

- Montañez, I. P. & Poulsen, C. J. The Late Paleozoic Ice Age: An evolving paradigm. *Annu. Rev. Earth Planet. Sci.* **41**, 629–656 (2013).
- Scotese, C. R. An Atlas of Phanerozoic paleogeographic maps: The seas come in and the seas go out. *Annu. Rev. Earth Planet. Sci.* **49**, 679–728 (2021).
- Chen, J. et al. Marine anoxia linked to abrupt global warming during Earth's penultimate icehouse. *Proc. Natl. Acad. Sci. USA.* **119**, e2115231119 (2022).
- Matthews, K. J. et al. Global plate boundary evolution and kinematics since the late Paleozoic. *Glob. Planet. Change* <https://doi.org/10.1016/j.gloplacha.2016.10.002> (2016).
- McKenzie, N. R. et al. Continental arc volcanism as the principal driver of icehouse-greenhouse variability. *Science* **352**, 444–447 (2016).
- Jurikova, H. et al. Rapid rise in atmospheric CO₂ marked the end of the Late Palaeozoic Ice Age. *Nat. Geosci.* **18**, 91–97 (2025).
- Kent, D. V. & Muttoni, G. Pangea B and the Late Paleozoic Ice Age. *Palaeogeogr. Palaeoclimatol., Palaeoecol.* **553**, 109753 (2020).
- Zou, C. et al. Organic-matter-rich shales of China. *Earth-Sci. Rev.* **189**, 51–78 (2019).
- Foster, G. L., Royer, D. L. & Lunt, D. J. Future climate forcing potentially without precedent in the last 420 million years. *Nat. Commun.* **8**, 14845 (2017).
- Judd, E. J. et al. A 485-million-year history of Earth's surface temperature. *Science* **385**, eadk3705 (2024).
- Feulner, G. Formation of most of our coal brought Earth close to global glaciation. *Proc. Natl. Acad. Sci. USA.* **114**, 11333–11337 (2017).
- Conrad, C. P. The solid Earth's influence on sea level. *Geol. Soc. Am. Bull.* **125**, 1027–1052 (2013).
- Merdith, A. S. et al. Extending full-plate tectonic models into deep time: Linking the Neoproterozoic and the Phanerozoic. *Earth-Sci. Rev.* **214**, 103477 (2021).
- Cerpa, N. G., Rees Jones, D. W. & Katz, R. F. Consequences of glacial cycles for magmatism and carbon transport at mid-ocean ridges. *Earth Planet. Sci. Lett.* **528**, 115845 (2019).
- Müller, R. D. & Dutkiewicz, A. Oceanic crustal carbon cycle drives 26-million-year atmospheric carbon dioxide periodicities. *Sci. Adv.* **4**, eaaq0500 (2018).
- Hu, Y. et al. Emergence of the modern global monsoon from the Pangea megamonsoon set by palaeogeography. *Nat. Geosci.* <https://doi.org/10.1038/s41561-023-01288-y> (2023).
- Laskar, J. et al. A long-term numerical solution for the insolation quantities of the Earth. *AA* **428**, 261–285 (2004).
- Hinnov, L. A. Cyclostratigraphy and its revolutionizing applications in the earth and planetary sciences. *Geol. Soc. Am. Bull.* **125**, 1703–1734 (2013).
- Meyers, S. Cracking the palaeoclimate code. *Nature* **546**, 219–220 (2017).
- Li, M. et al. Paleoclimate proxies for cyclostratigraphy: Comparative analysis using a Lower Triassic marine section in South China. *Earth-Sci. Rev.* **189**, 125–146 (2019).
- Wang, M. et al. Astronomical forcing and sedimentary noise modeling of lake-level changes in the Paleogene Dongpu Depression of North China. *Earth Planet. Sci. Lett.* **535**, 116116 (2020).
- Cao, W. Episodic nature of continental arc activity since 750 Ma: A global compilation. *Earth Planet. Sci. Lett.* <https://doi.org/10.1016/j.epsl.2016.12.044> (2017).
- Wu, H. et al. Astronomical time scale for the Paleozoic Era. *Earth-Sci. Rev.* **244**, 104510 (2023).
- Wei, R. et al. Obliquity forcing of continental aquifers during the late Paleozoic ice age. *Earth Planet. Sci. Lett.* **613**, 118174 (2023).
- Jiang, Q., Jourdan, F., Olierook, H. K. H. & Merle, R. E. An appraisal of the ages of Phanerozoic large igneous provinces. *Earth-Sci. Rev.* **237**, 104314 (2023).
- Farhat, M., Laskar, J. & Boué, G. Constraining the Earth's dynamical ellipticity from ice age dynamics. *J. Geophys. Res.: Solid Earth* **127**, (2022).
- Mitrovica, J. X. et al. Dynamic Topography and Ice Age Paleoclimate. *Annu. Rev. Earth Planet. Sci.* **48**, 585–621 (2020).
- Voice, P. J., Kowalewski, M. & Eriksson, K. A. Quantifying the Timing and Rate of Crustal Evolution: Global Compilation of Radiometrically Dated Detrital Zircon Grains. *J. Geol.*
- Roberts Nick, M. W. & Spencer Christopher, J. The zircon archive of continent formation through time. *Geol. Soc. Lond. Spec. Publ.* **389**, 197–225 (2015).

30. Palmer, M. R. & Edmond, J. M. The strontium isotope budget of the modern ocean. *Earth Planet. Sci. Lett.* **92**, 11–26 (1989).
31. Banner, J. L. Radiogenic isotopes: systematics and applications to earth surface processes and chemical stratigraphy. *Earth-Sci. Rev.* **65**, 141–194 (2004).
32. Zeebe, R. E. LOSCAR: Long-term Ocean-atmosphere-Sediment Carbon cycle Reservoir Model v2.0.4. *Geosci. Model Dev.* **5**, 149–166 (2012).
33. Papadomanolaki, N. M., Van Helmond, N. A. G. M., Paelike, H., Sluijs, A. & Slomp, C. P. *Quantifying Volcanism and Organic Carbon Burial across Oceanic Anoxic Event 2& #160*; <https://meetingorganizer.copernicus.org/EGU22/EGU22-4796.html>, <https://doi.org/10.5194/egusphere-egu22-4796> (2022).
34. Heimdal, T. H., Jones, M. T., Svensen & Henrik, H. Thermogenic carbon release from the Central Atlantic magmatic province caused major end-Triassic carbon cycle perturbations. *Proc. Natl. Acad. Sci. USA* **117**, 11968–11974 (2020).
35. Horton, D. E., Poulsen, C. J. & Pollard, D. Orbital and CO₂ forcing of late Paleozoic continental ice sheets. *Geophys. Res. Lett.* **34**, L19708 (2007).
36. Majorowicz, J., Grasby, S. E., Safanda, J. & Beauchamp, B. Gas hydrate contribution to Late Permian global warming. *Earth Planet. Sci. Lett.* **393**, 243–253 (2014).
37. Wang, W. et al. Ecosystem responses of two Permian biocrises modulated by CO₂ emission rates. *Earth Planet. Sci. Lett.* **602**, 117940 (2023).
38. Boulila, S. et al. On the origin of Cenozoic and Mesozoic “third-order” eustatic sequences. *Earth-Sci. Rev.* **109**, 94–112 (2011).
39. Wright, N. M., Seton, M., Williams, S. E., Whittaker, J. M. & Müller, R. D. Sea-level fluctuations driven by changes in global ocean basin volume following supercontinent break-up. *Earth-Sci. Rev.* **208**, 103293 (2020).
40. Li, M., Hinnov, L. A., Huang, C. & Ogg, J. G. Sedimentary noise and sea levels linked to land–ocean water exchange and obliquity forcing. *Nat. Commun.* **9**, 1004 (2018).
41. Huybers, P. Early Pleistocene glacial cycles and the integrated summer insolation forcing. *Science* **313**, 508–511 (2006).
42. Wei, R. et al. Orbitally-paced coastal sedimentary records and global sea-level changes in the early Permian. *Earth Planet. Sci. Lett.* **620**, 118356 (2023).
43. Van der Meer, D. et al. Plate tectonic controls on atmospheric CO₂ levels since the Triassic. *Proc. Natl. Acad. Sci. USA* **111**, 4380–4385 (2014).
44. Ma, C., Meyers, S. R. & Sageman, B. B. Theory of chaotic orbital variations confirmed by Cretaceous geological evidence. *Nature* **542**, 468–470 (2017).
45. Holbourn, A. E. et al. Late Miocene climate cooling and intensification of Southeast Asian winter monsoon. *Nat. Commun.* **9**, 1584 (2018).
46. Zuidema, P. A. et al. Tropical tree growth driven by dry-season climate variability. *Nat. Geosci.* **15**, 269–276 (2022).
47. Ridgwell, A. & Zeebe, R. E. The role of the global carbonate cycle in the regulation and evolution of the Earth system. *Earth Planet. Sci. Lett.* **234**, 299–315 (2005).
48. Calvin, K. et al. *IPCC, 2023: Climate Change 2023: Synthesis Report. Contribution of Working Groups I, II and III to the Sixth Assessment Report of the Intergovernmental Panel on Climate Change [Core Writing Team, H. Lee and J. Romero (Eds.)]. IPCC, Geneva, Switzerland.* <https://www.ipcc.ch/report/ar6/syr/>, <https://doi.org/10.59327/IPCC/AR6-9789291691647> (2023).
49. Gaillardet, J., Dupré, B., Louvat, P. & Allègre, C. J. Global silicate weathering and CO₂ consumption rates deduced from the chemistry of large rivers. *Chem. Geol.* **159**, 3–30 (1999).
50. Kump, L. R., Brantley, S. L. & Arthur, M. A. Chemical weathering, atmospheric CO₂, and climate. *Annu. Rev. Earth Planet. Sci.* **28**, 611–667 (2000).
51. Landwehrs, J., Feulner, G., Petri, S., Sames, B. & Wagreich, M. Investigating mesozoic climate trends and sensitivities with a large ensemble of climate model simulations. *Paleoceanog. Paleoclimatol.* **36**, e2020PA004134 (2021).
52. Yuan, S. et al. Controlling factors for the global meridional overturning circulation: A lesson from the Paleozoic. *Sci. Adv.* **10**, eadm7813 (2024).
53. Zhang, S. et al. The Hadley circulation in the Pangea era. *Sci. Bull.* **68**, 1060–1068 (2023).
54. Huang, H. et al. Organic carbon burial is paced by a -173-ka obliquity cycle in the middle to high latitudes. *Sci. Adv.* **7**, eabf9489 (2021).
55. Alley, R. B. et al. Abrupt climate change. *Science* **299**, 7 (2003).
56. De Vleeschouwer, D., Percival, L. M. E., Wichern, N. M. A. & Batenburg, S. J. Pre-Cenozoic cyclostratigraphy and palaeoclimate responses to astronomical forcing. *Nat. Rev. Earth Environ.* **5**, 59–74 (2024).
57. Shen, J. et al. Intensified continental chemical weathering and carbon-cycle perturbations linked to volcanism during the Triassic–Jurassic transition. *Nat. Commun.* **13**, 299 (2022).
58. Frogner, P., Gislason, S. R. & Óskarsson, N. Fertilizing potential of volcanic ash in ocean surface water. *Geology* **29**, 487–490 (2001).
59. Black, B. A. et al. Systemic swings in end-Permian climate from Siberian Traps carbon and sulfur outgassing. *Nat. Geosci.* **11**, 949–954 (2018).
60. Landwehrs, J. P., Feulner, G., Hofmann, M. & Petri, S. Climatic fluctuations modeled for carbon and sulfur emissions from end-Triassic volcanism. *Earth Planet. Sci. Lett.* **537**, 116174 (2020).
61. Wignall, P. B. Large igneous provinces and mass extinctions. *Earth-Sci. Rev.* **53**, 1–33 (2001).
62. Zachos, J., Pagani, M., Sloan, L., Thomas, E. & Billups, K. Trends, rhythms, and aberrations in global climate 65 Ma to present. *Science* **292**, 686–693 (2001).
63. Horton, D. E., Poulsen, C. J. & Pollard, D. Influence of high-latitude vegetation feedbacks on late Palaeozoic glacial cycles. *Nat. Geosci.* **3**, 572–577 (2010).
64. Horton, D. E., Poulsen, C. J., Montañez, I. P. & DiMichele, W. A. Eccentricity-paced late Paleozoic climate change. *Palaeogeogr. Palaeoclimatol. Palaeoecol.* **331–332**, 150–161 (2012).
65. Van Peer, T. E. et al. Eccentricity pacing and rapid termination of the early Antarctic ice ages. *Nat. Commun.* **15**, 10600 (2024).
66. Hobart, B., Lisiecki, L. E., Rand, D., Lee, T. & Lawrence, C. E. Late Pleistocene 100-kyr glacial cycles paced by precession forcing of summer insolation. *Nat. Geosci.* **16**, 717–722 (2023).
67. Sarr, A. et al. Ventilation changes drive orbital-scale deoxygenation trends in the late Cretaceous ocean. *Geophys. Res. Lett.* **49**, e2022GL099830 (2022).
68. Frank, D. et al. Effects of climate extremes on the terrestrial carbon cycle: concepts, processes and potential future impacts. *Glob. Change Biol.* **21**, 2861–2880 (2015).
69. Walsh, J. E. et al. Extreme weather and climate events in northern areas: A review. *Earth-Sci. Rev.* **209**, 103324 (2020).
70. Konapala, G., Mishra, A. K., Wada, Y. & Mann, M. E. Climate change will affect global water availability through compounding changes in seasonal precipitation and evaporation. *Nat. Commun.* **11**, 3044 (2020).
71. Montañez, I. P. et al. Climate, pCO₂ and terrestrial carbon cycle linkages during late Palaeozoic glacial–interglacial cycles. *Nat. Geosci.* **9**, 824–828 (2016).
72. Dahl, T. W. & Arens, S. K. M. The impacts of land plant evolution on Earth’s climate and oxygenation state – An interdisciplinary review. *Chem. Geol.* **547**, 119665 (2020).

73. Cleal, C. J. & Thomas, B. A. Palaeozoic tropical rainforests and their effect on global climates: is the past the key to the present?. *Geobiology* **3**, 13–31 (2005).
74. Lange, M., Eisenhauer, N., Chen, H. & Gleixner, G. Increased soil carbon storage through plant diversity strengthens with time and extends into the subsoil. *Glob. Change Biol.* **29**, 2627–2639 (2023).
75. Hurrell, J. W. et al. The Community Earth System Model: A framework for collaborative research. *Bull. Am. Meteorol. Soc.* **94**, 1339–1360 (2013).
76. Neale, R. B. et al. The mean climate of the community atmosphere model (CAM4) in forced SST and fully coupled experiments. *J. Clim.* **26**, 5150–5168 (2013).
77. Lawrence, D. M. et al. The CCSM4 land simulation, 1850–2005: Assessment of surface climate and new capabilities. *J. Clim.* **25**, 2240–2260 (2012).
78. Smith, R., Jones, P., Briegleb, B., Bryan, F. & Yeager, S. The Parallel Ocean Program (POP) reference manual: Ocean component of the Community Climate System Model (CCSM). (2010).
79. Hunke, E. C. & Lipscomb, W. H. CICE: the Los Alamos Sea Ice Model Documentation and Software User’s Manual Version 4. (2010).
80. Schmidt, H. et al. Solar irradiance reduction to counteract radiative forcing from a quadrupling of CO₂: climate responses simulated by four Earth system models. *Earth Syst. Dynam.* **3**, 63–78 (2012).
81. Cramer, B. D. & Jarvis, I. Carbon Isotope Stratigraphy. in *Geologic Time Scale 2020* 309–343 (Elsevier, 2020). <https://doi.org/10.1016/B978-0-12-824360-2.00011-5>.
82. Feng, W. et al. Volcanic CO₂ emissions from subduction of the tropical Paleo-Tethyan Ocean contributed to the early Permian deglacial warming. *Earth Planet. Sci. Lett.* **660**, 119361 (2025).
83. Wei, R. et al. Tectonic–astronomical interactions in shaping late Paleozoic climate and organic carbon burial [Data set]. Zenodo <https://doi.org/10.5281/zenodo.15645982> (2025).
84. Scotese, C. R. PALEOMAP PaleoAtlas for GPlates and the PaleoData Plotter Program. *PALEOMAP Project* (2016).
85. Haq, B. U. & Schutter, S. R. A chronology of Paleozoic sea-level changes. *Science* **322**, 64–68 (2008).
86. Cong, F. et al. Orbitally forced glacio-eustatic origin of third-order sequences and parasequences in the Middle Permian Maokou Formation, South China. *Mar. Pet. Geol.* **99**, 237–251 (2019).
87. Lu, C. et al. Geochemical constraints and astronomical forcing on organic matter accumulation of marine–continental transitional shale deposits in the Qinshui Basin during the Carboniferous–Permian Transition. *ACS Earth Space Chem.* **8**, 616–629 (2024).
88. Stothers, R. B. Linear and circular digital spectral analysis of serial data. *Astrophys. J.* 423–426 (1991).
89. Rampino, M. R., Caldeira, K. & Zhu, Y. A pulse of the Earth: A 27.5-Myr underlying cycle in coordinated geological events over the last 260 Myr. *Geosci. Front.* **12**, 101245 (2021).
90. Li, M., Hinnov, L. & Kump, L. Acycle: Time-series analysis software for paleoclimate research and education. *Comput. Geosci.* **127**, 12–22 (2019).
91. Richey, J. D. et al. Influence of temporally varying weatherability on CO₂-climate coupling and ecosystem change in the late Paleozoic. *Clim. Past* **16**, 1759–1775 (2020).
92. Ernst, R. E. Large Igneous Provinces. In *Large Igneous Provinces* (ed. Ernst, R. E.) iii–iii (Cambridge University Press, Cambridge, 2014).
93. Buggisch, W., Wang, X., Alekseev, A. S. & Joachimski, M. M. Carboniferous–Permian carbon isotope stratigraphy of successions from China (Yangtze platform), USA (Kansas) and Russia (Moscow Basin and Urals). *Palaeogeogr. Palaeoclimatol. Palaeoecol.* **301**, 18–38 (2011).
94. Grossman, E. L. & Joachimski, M. M. Ocean temperatures through the Phanerozoic reassessed. *Sci. Rep.* **12**, 8938 (2022).

Acknowledgements

This work was supported by the National Natural Science Foundation of China (grant nos. 42090025 and 42488101 to Z.J., and 42488201 to Y.H.), the China Postdoctoral Science Foundation (grant no. BX20240020 to R.W.), and the High-Performance Computing Platform of Peking University. This study also contributes to the Deep-time Digital Earth Big Science Program.

Author contributions

R.W. and Z.J. conceived and designed the study. R.W. conducted the climate model simulations, performed the data analysis, and drafted the manuscript. R.W., Z.J., M.L., S.Y., Y.H., L.D., R.Z., and J.S. contributed to data interpretation, discussion, and manuscript revision.

Competing interests

The authors declare no competing interests.

Additional information

Supplementary information The online version contains supplementary material available at <https://doi.org/10.1038/s41467-025-63896-z>.

Correspondence and requests for materials should be addressed to Zhijun Jin.

Peer review information *Nature Communications* thanks the anonymous reviewer(s) for their contribution to the peer review of this work. A peer review file is available.

Reprints and permissions information is available at <http://www.nature.com/reprints>

Publisher’s note Springer Nature remains neutral with regard to jurisdictional claims in published maps and institutional affiliations.

Open Access This article is licensed under a Creative Commons Attribution-NonCommercial-NoDerivatives 4.0 International License, which permits any non-commercial use, sharing, distribution and reproduction in any medium or format, as long as you give appropriate credit to the original author(s) and the source, provide a link to the Creative Commons licence, and indicate if you modified the licensed material. You do not have permission under this licence to share adapted material derived from this article or parts of it. The images or other third party material in this article are included in the article’s Creative Commons licence, unless indicated otherwise in a credit line to the material. If material is not included in the article’s Creative Commons licence and your intended use is not permitted by statutory regulation or exceeds the permitted use, you will need to obtain permission directly from the copyright holder. To view a copy of this licence, visit <http://creativecommons.org/licenses/by-nc-nd/4.0/>.

© The Author(s) 2025, modified publication 2025